

# Refinement and Experimental Validation of a Vacancy Model of Pore Annihilation in Single-Crystal Nickel-Base Superalloys during Hot Isostatic Pressing

Alexander Epishin, Bettina Camin,\* Lennart Hansen, Marek Heuser, Inmaculada Lopez-Galilea, Benjamin Rutttert, Werner Theisen, and Bernard Fedelich

Initially, as-cast and homogenized single crystals of nickel-base superalloy CMSX-4 are subjected to hot isostatic pressing at 1288 °C. Two series of experiments are conducted: under the same pressure of 103 MPa but with different durations, between 0.5 and 6 h, and under different pressures, between 15 and 150 MPa, but for the same time of 0.5 h. The porosity annihilation is investigated metallographically and by high-resolution synchrotron X-ray tomography. The obtained experimental results are compared with the predictions of the vacancy model proposed recently in the group. Herein, the model is further refined by coupling with X-ray tomography. The model describes the evolution of the pore arrays enclosed in the 3D synchrotron tomograms during hot isostatic pressing and properly predicts the time and stress dependences of the pore annihilation kinetics. The validated model and the obtained experimental results are used for selecting the optimal technological parameters such as applied pressure and processing time.


## 1. Introduction

Turbine blades are critical components of aircraft jet engines and gas power plants because they operate at high temperatures

Dr. A. Epishin, Dr. B. Camin, L. Hansen, M. Heuser  
Faculty III Process Sciences  
Institute of Material Sciences and Technology  
Chair of Metallic Materials  
Technische Universität Berlin  
Sekt. BH18, Ernst-Reuter-Platz 1, 10587 Berlin, Germany  
E-mail: camin@physik.tu-berlin.de

Dr. I. Lopez-Galilea, Dr. B. Rutttert, Prof. W. Theisen  
Institute for Materials  
Ruhr University of Bochum  
Universitätsstr. 150, 44801 Bochum, Germany

Dr. B. Fedelich  
Department of Materials Engineering  
Federal Institute for Materials Research and Testing (BAM)  
Unter den Eichen 87, 12205 Berlin, Germany

 The ORCID identification number(s) for the author(s) of this article can be found under <https://doi.org/10.1002/adem.202100211>.

© 2021 The Authors. Advanced Engineering Materials published by Wiley-VCH GmbH. This is an open access article under the terms of the Creative Commons Attribution License, which permits use, distribution and reproduction in any medium, provided the original work is properly cited.

DOI: 10.1002/adem.202100211

under mechanical loads of different types in an aggressive environment. Therefore, the turbine blades are cast from nickel-base superalloys possessing excellent service properties at high temperatures.<sup>[1]</sup> To improve their creep strength and corrosion resistance, hot section turbine blades are commonly produced as single crystals by directional solidification<sup>[2]</sup> and are therefore free of damaging high-angle grain boundaries. However, application of this advanced technology cannot avoid such a detrimental microstructural defect as microporosity.

Microporosity forms in single-crystal blades during the different steps of their manufacturing as well as in service. The initial porosity develops during dendritic solidification of blades due to insufficient afflux of melt into the interdendritic

regions.<sup>[3,4]</sup> These pores have an irregular shape, can branch, and extend up to a few hundred micrometers in length. **Figure 1a** shows a crack initiated at such a pore during low-cycle fatigue test of a single crystal of superalloy CMSX-4 at 700 °C,<sup>[5]</sup> which eventually led to specimen failure. Such large pores are quite rare, but they are very dangerous. The next type of porosity forms during homogenization heat treatment. The formation of these pores was considered in various studies,<sup>[6–8]</sup> and it was shown that the main mechanism of porosity growth during homogenization is vacancy flux toward the dissolving nonequilibrium eutectics compensating the counterdiffusion of fast aluminum atoms (Kirkendall effect).<sup>[8]</sup> These pores have round shape with diameter of about 10 μm, see **Figure 1**. The third type of porosity develops during long-term high-temperature deformation (creep), which occurs under service conditions. This porosity is represented by small, faceted pores of a few micrometers in size, see **Figure 1c**. Because of their crystallographic shape, such pores are called as “negative crystals.”<sup>[9]</sup> The growth of these pores in single-crystal superalloys was reported in many papers,<sup>[10–13]</sup> and it was shown that they form by condensation of vacancies emitted by the edge parts of dislocations climbing along the  $\gamma/\gamma'$  interfaces.<sup>[13]</sup> It is proposed to call the types of pores mentioned earlier, respectively, as solidification (S), homogenization (H), and deformation (D) pores.<sup>[14]</sup>

S and H porosity in single-crystal nickel-base superalloys can be reduced by selecting the optimal parameters of directional

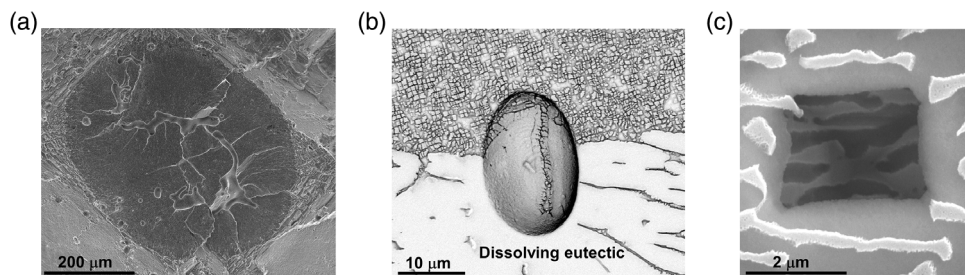


**Figure 1.** Different types of pores in single-crystal nickel-base superalloys, as shown by SEM. a) Branching S pore in CMSX-4 initiated fatigue failure at 700 °C. b) Round H pore in CMSX-10 after 16 h homogenization at 1340 °C. c) D pore (“negative crystal”) in CMSX-4 after 292 h creep at 1100 °C and 120 MPa.

solidification and homogenization heat treatment<sup>[4,15]</sup> but a complete removal of the pores is only possible by applying a hot isostatic pressing (HIP) treatment to the components. Effects of HIP on the mechanical properties and microstructure of single-crystal superalloys were investigated widely.<sup>[16–24]</sup> It was found that removing the pores by HIP dramatically increases the fatigue life, whereas the other mechanical properties are hardly altered.<sup>[16,17,22]</sup> The reason for the first effect is that under cycling loading, the stress concentrations near the pores result in enhanced local strain amplitudes, leading to the nucleation of fatigue cracks.

HIP of the single-crystal blades is usually conducted in a narrow temperature window, between the  $\gamma'$  solvus and the solidus, in which the strengthening  $\gamma'$  phase is totally dissolved, and the blade material is very soft. However, such a high-temperature process can damage a costly blade by recrystallization and incipient melting. Therefore, the parameters of commercial HIP (temperature  $T$ , pressure  $p$ , and duration  $t$ ) have to be carefully optimized under the conditions of full pore healing, avoidance of material damage, and minimal processing costs. The HIP parameters can be optimized using a reliable physical model validated by HIP experiments conducted under different HIP conditions.

Two models, based on different pore closure mechanisms, were proposed: a model of the pore closure by dislocation creep<sup>[25]</sup> and a model of the pore dissolution by emission of vacancies.<sup>[26]</sup> More promising preliminary results were obtained by the vacancy model (VM), whereas the creep model significantly overestimated the porosity annihilation rate. Therefore, in this work, the VM was considered and applied. This VM assumes that under applied pressure, the low-angle boundaries (LABs) operate as sinks of vacancies emitted by the surface of shrinking pores. As a result of this process, the pores gradually shrink and heal.

The aim of the present work is the experimental investigation of the porosity annihilation in single-crystal superalloy CMSX-4 during HIP as well as refinement and validation of the proposed VM. The residual porosity in HIPed samples has been investigated metallographically in 2D sections and 3D by high-resolution synchrotron X-ray computer tomography (XCT). In a previous work, we used XCT to investigate microporosity in single-crystal nickel-base superalloys in as-cast, heat-treated, and deformed (after creep) conditions, and these investigations demonstrated the high efficiency of this technique for porosity

characterization.<sup>[27]</sup> Now, we have applied this method to investigate porosity annihilation during HIP.

## 2. Experimental Section

### 2.1. Material and Experimental Methods

The material under investigation is the single-crystal nickel-base superalloy CMSX-4<sup>[28]</sup> developed by the Cannon & Muskegon Corporation, USA, and widely used for casting gas turbine blades. The alloy contains 3 wt% Re (see Table 1) and according to the international classification belongs to the second generation of single-crystal superalloys. Single-crystal bars of CMSX-4 with axial orientation [001] were solidified by Howmet Alcoa, USA. The microporosity was measured in the bottom, middle, and top of these bars and was found to be quite homogeneous. Some bars were left in the as-cast condition, others were subjected to the standard solution heat treatment (homogenized). With an accuracy of  $\pm 3$ –4 °C, all HIP experiments were conducted at 1288 °C, which is the temperature at which HIP is commercially applied to CMSX-4 by Howmet Alcoa. This temperature was slightly above the  $\gamma'$  solvus temperature of CMSX-4 but significantly lower than its solidus temperature, respectively, equal to 1282 and 1339 °C.<sup>[2]</sup> Two series of HIP experiments were conducted. 1) HIP experiments of different durations, 0.5, 1, 2, 4, and 6 h, under the pressure of 103 MPa (corresponding to the commercial HIP procedure). 2) HIP experiments of the same duration, 0.5 h, but under different pressures between 15 and 150 MPa.

The first series of HIP experiments was conducted in an industrial HIP plant QIH-16 ASEA at the All-Russian Institute of Aviation Materials (VIAM), Moscow, Russia. The second series was conducted in a research HIP press QIH-9 QUINTUS at the Ruhr-University of Bochum (RUB), Germany.

Residual porosity in the samples from the first HIP series was previously characterized by optical microscopy (OM), scanning electron microscopy (SEM), and density measurement

**Table 1.** Nominal composition of superalloy CMSX-4.

Element	Al	Ti	Cr	Co	Ni	Mo	Ta	W	Re
wt%	5.7	1.0	6.4	9.7	base	0.6	6.5	6.4	3.0
at%	12.82	1.27	7.47	9.99	base	0.38	2.18	2.11	0.98

(DM).<sup>[21,22]</sup> In the present work, it was investigated by high-resolution XCT. For tomographic imaging of microporosity, small needle-shaped samples were cut by spark erosion. The samples had a diameter of 1 mm and a length of 10 mm. Due to the dendritic spacing of about 0.35 mm, every sample contained about eight dendrites, which was sufficient to exclude the effect of dendritic inhomogeneity on the obtained results. The tomographic measurements were carried out at the beamline ID19 at the European Synchrotron Radiation Facility (ESRF) in Grenoble, France. A monochromatic X-ray beam with an energy of 70 keV at a current of 200 mA (7/8 multibunch mode) was used. The radiographs were recorded in absorption and phase contrasts with a sCMOS camera PCO EDGE 4.2, exhibiting a resolution of 2048 × 2048 pixel. The continuous 360° rotation of the sample enabled an effective measuring field of 3700 × 3700 × 2048 voxel with spatial image sizes of 1265 × 1265 × 700 μm<sup>3</sup>. This corresponded to a submicrometer resolution of 0.347<sup>3</sup> μm<sup>3</sup> per voxel in the reconstructed 3D tomograms. During one complete rotation of the sample, about 5000 radiographs were recorded with an exposure time of 50 ms per radiograph. Thus, the total measuring time was about 5 min per tomogram. The reconstructed tomograms were evaluated with the defect analysis tool of the commercial visualization software VGStudio Max (Version 2.1) from the company Volume Graphics.<sup>[29]</sup>

Processing of the porosity tomograms with this software provides arrays of data containing geometrical parameters for every pore, including in particular the pore identification number  $i$ , pore position,  $(x, y, z)_i$ , pore volume  $V_{p,i}$ , and the projection areas on the coordinate planes  $PX_{p,i}$ ,  $PY_{p,i}$ ,  $PZ_{p,i}$ . The porosity volume fraction is determined as

$$f_p = V_T^{-1} \sum_i V_{p,i} \quad (1)$$

where  $V_T$  is the analyzed specimen volume.

In the refined VM used in this work, a correction of the pore surface  $S_{p,i}$  due to deviation of the pore shape from the spherical shape has to be considered. This effect can be accounted for using the inverse of Wadell's sphericity factor<sup>[30]</sup> as a corrective term.

$$\psi_{p,i}^{-1} = S_{p,i}/S_{\text{sphere}}(V_{p,i}) \quad \text{with} \quad S_{\text{sphere}}(V_{p,i}) = \pi^{1/3}(6V_{p,i})^{2/3} \quad (2)$$

However, the available software VGStudio Max (Version 2.1) represents the objects by voxels (as stepped surface), which leads to significant overestimation of  $S_{p,i}$  and consequently of  $\psi_{p,i}^{-1}$ . For example, for a spherical object, the software gives  $\psi^{-1} = 1.5$  instead of 1. To reduce the error of  $\psi^{-1}$  measurement, it was proposed in the study by Rothleitner et al.<sup>[31]</sup> to approximate  $S_{p,i}$  as

$$S_{p,i} = 4\bar{A}_{p,i} \quad (3)$$

where  $\bar{A}_{p,i}$  is the mean projection area defined by

$$\bar{A}_{p,i} = \frac{(PX_{p,i} + PY_{p,i} + PZ_{p,i})}{3} \quad (4)$$

This approximation has been used in our work.

Residual porosity in the samples HIPed in the second series of HIP experiments was investigated by SEM. From every sample, 81 backscatter electron (BSE) and 81 secondary electron (SE) images were taken, covering the area of  $2.9 \times 3.9 = 11.3 \text{ mm}^2$ , which corresponded to about 90 dendritic cells. Simultaneous BSE and SE imaging of every area is necessary to distinguish the pores from other objects. The SEM images were analyzed with the image processing program ImageJ.<sup>[32]</sup> Automatic image binarization revealed objects different from pores; therefore, every binarized image was subsequently manually corrected to exclude these artifacts. It should be mentioned that the porosity was quantified in sections, so the area fraction of pores was the quantity that was actually characterized. However, as the pores from different geometries were randomly arranged in the volume, in any selected 2D cutting plane, the area fraction of pores corresponded to the 3D volume fraction.<sup>[33,34]</sup> Therefore, hereafter, the area fraction of pores measured by SEM and OM will be referred to as the volume fraction  $f_p$ .

## 2.2. Vacancy Model

The proposed VM<sup>[26]</sup> assumes that under an external pressure  $p$  applied during HIP, the vacancy concentration at the cores of edge dislocations forming the LAB  $C_{\text{LAB}}$  decreases below the equilibrium value  $C^0$  according to

$$C_{\text{LAB}} = C^0 \exp\left(-\frac{pV_a}{kT}\right) \quad (5)$$

where  $V_a$  is the atomic volume,  $k$  the Boltzmann constant, and  $T$  the absolute temperature. In contrast, the vacancy concentration is equal to its equilibrium value  $C^0$  at the surface of the gas-free pore.

This results in the vacancy concentration gradient  $\frac{(C_{\text{LAB}} - C^0)}{R_s - R_p}$  between the LAB and the pore, which activates a vacancy flux from the pore to the LAB, as shown in **Figure 2**. The pore emits vacancies and gradually shrinks, whereas the LAB operates as a vacancy sink. One can get an analytical solution for the kinetics of pore shrinkage assuming 1) spherical symmetry; 2) stationary

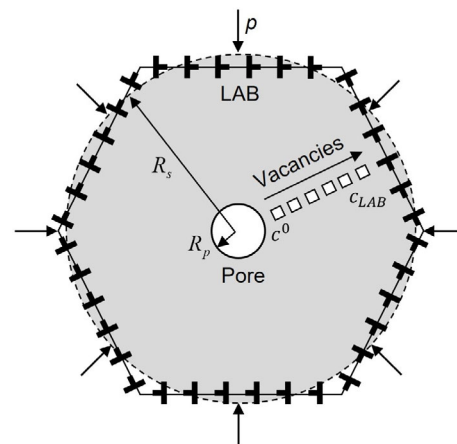


**Figure 2.** A model for vacancy dissolution of pores during HIP: a subgrain with a central pore bordered by LAB consisting of edge dislocations.

vacancy diffusion,  $\partial c(r, t)/\partial t = 0$ ; and 3)  $R_p \ll R_s$ , where  $R_p$  and  $R_s$  are, respectively, the radii of the pore and the subgrain.

It should be mentioned that the last assumption is reasonable for materials with low porosity, which is the case of single-crystal superalloys, where the porosity volume fraction  $f_p$  is typically between 0.1 and 0.2 vol. %.

The following analytical solution was derived in the study by Epishin et al.<sup>[26]</sup>

$$R_p^2(t) = R_p^2(0) - k_R t \quad \text{with} \quad k_R = 2 \frac{D_{Ni}^{Ni} V_a}{\xi k T} p \quad (6)$$

where  $D_{Ni}^{Ni}$  is the self-diffusion coefficient of base element Ni,  $\xi$  the correlation factor for diffusion in the face centered cubic lattice, and  $t$  is the time elapsed since beginning of the HIP process. It is assumed in Equation (6) that the LABs are perfect vacancy sinks. In other words, the LAB is assumed to be equivalent to a free surface.

One of the most important geometrical parameters of a pore is its volume  $V_p$ . The pore volume was directly measured by XCT as opposed to the widely used equivalent radius (or diameter), which is a parameter derived from  $V_p$ . Therefore, for coupling XCT with diffusion modeling, it is reasonable to change the variable in Equation (6) from the pore radius  $R_p$  to the originally measured pore volume  $V_p$ . Performing this change, one gets

$$V_p^{2/3}(t) = V_p^{2/3}(0) - k_v t \quad \text{with} \quad k_v = 8 \left(\frac{\pi}{6}\right)^{2/3} \frac{D_{Ni}^{Ni} V_a}{\xi k T} p \quad (7)$$

Equation (7) is derived under the assumption that all pores in the material are spherical and have the same volume initially equal to the average pore volume  $\bar{V}_p(0)$  in unHIPed material. However, as shown later, a prediction under this assumption overestimates the porosity annihilation rate. Therefore, for an adequate description of the porosity annihilation during HIP, the pore volume distribution has to be considered. It is seen that Equation (7) is independent from the boundary conditions and thus can be applied independently to every individual  $i$ th pore of volume  $V_{p,i}$  in the porosity tomogram.

$$V_{p,i}^{2/3}(t) = V_{p,i}^{2/3}(0) - k_v t \quad (8)$$

However, Equation (8) does not take into account that the pore shape can deviate from the spherical shape, which increases the pore surface  $S_{p,i}$  emitting vacancies. This shape effect can be considered by introducing the inverse sphericity factor  $\psi_{p,i}^{-1}$ , as defined in Equation (2). The factor  $k_v$  in Equation (8) describes the vacancy emission rate integrated over the spherical pore surface. Therefore, for nonspherical pores with larger surface area  $S_{p,i}$ , the rate factor  $k_v$  should be accordingly higher. This can be considered by multiplying  $k_v$  by  $\psi_{p,i}^{-1}$ . In a first approximation, it has been assumed that the pores shrink keeping their shape, that is,  $\psi_{p,i}^{-1}(t) = \psi_{p,i}^{-1}(0)$ . Thus, Equation (8) can be modified as

$$V_{p,i}^{2/3}(t) = V_{p,i}^{2/3}(0) - \psi_{p,i}^{-1}(0) k_v t \quad (9)$$

Computing the change of  $V_{p,i}(t)$  in time with Equation (9), one can predict the change of porosity volume fraction  $f_p(t)$  (as defined by Equation (1)), the evolution of histogram of the

pore size (e.g., equivalent diameter  $D_{p,i}^{eq} = (6V_{p,i}/\pi)^{1/3}$ ), the time to the complete pore closure, etc.

In the calculations carried out in this work, the following values for the parameters of Equation (7) have been used:  $D_{Ni}^{Ni}(T) = \exp(\Delta G/RT)$ ,  $m^2 s^{-1}$  with  $\Delta G = -287\,000 - 69.8 \times T$ ,  $J mol^{-1}[35]$ , which gives  $D_{Ni}^{Ni}(1288^\circ C) = 5.62 \times 10^{-14} m^2 s^{-1}$ ,  $V_a = 1.25 \times 10^{-29} m^3$ ,<sup>[26]</sup> and  $\xi = 0.781$ .<sup>[36,37]</sup>

### 3. Results

The 3D tomographic images in **Figure 3** show the evolution of microporosity in the initially homogenized CMSX-4 during HIP at 1288 °C and 103 MPa. It is seen that porosity continuously decreases with HIPing time  $t$ . First, numerous small pores annihilate followed by less numerous large pores. This can be observed in the sequence of **Figure 3a–d,e** corresponding to HIPing durations 0, 0.5, 1, 2, and 4 h. After 4 h HIP (duration of commercial HIP applied to CMSX-4 by Howmet Alcoa), only rare pores of relatively small size remain. Such an unclosed pore marked by an arrow in **Figure 3e** is shown in **Figure 3f** at higher magnification. It is seen that this pore has an irregular shape, indicating that it originally is an S pore. The pore length is of about 36  $\mu m$  ( $D^{eq} = 23.5 \mu m$ ), which is much shorter than the length of a critical pore (a few hundred micrometers), as shown in **Figure 1a**.

**Figure 4** shows the kinetics of pore annihilation in CMSX-4, represented as  $f_p(t)$ , measured by the used experimental methods (OM, DM, XCT, and SEM) and predicted by the VM under different assumptions. **Figure 4a** shows  $f_p(t)$  for the initially as-cast condition and **Figure 4b** for the initially homogenized condition. The brown triangles and line in **Figure 4b** are OM measurements, the green squares and line in **Figure 4a,b** are DM measurements, the blue circles and lines in **Figure 4a** and **b** are XCT measurements, and the yellow diamond in **Figure 4b** is an SEM image. It is seen that all experimental methods give qualitatively similar results:  $f_p$  monotonically decreases during HIP with a decreasing slope  $|df_p(t)/dt|$ . They give also close  $f_p(0)$  values for the unHIPed material:  $f_p(0) \approx 0.12$  vol% for the as-cast condition and  $f_p(0) \approx 0.21$  vol% for the homogenized condition. However, with increasing HIP time  $t$ , some differences between the results of measurement methods appear. It is clear that OM (see **Figure 4b**) somewhat overestimates  $f_p$  compared with DM and XCT, which give very close  $f_p$  values. This difference obviously results from the lower spatial resolution of OM, which becomes critical when the pores decrease in size. Therefore, in the following, we will compare the theoretical predictions with the results of XCT, DM, and SEM.

The red lines in **Figure 4a,b** are predictions with the VM. The red dashed–dotted lines are predicted with Equation (7) under the assumption that all pores are spherical, with the same initial volume equal to the average pore value  $\bar{V}_p(0)$  in the unHIPed material, respectively, 146 and 420  $\mu m^3$  for as-cast and homogenized conditions, as evaluated from the corresponding tomograms. It is seen from **Figure 4a** and **b** that predictions with these initial values significantly overestimate the porosity annihilation rate  $|df_p(t)/dt|$ .

The prediction for  $f_p(t)$  can be improved by applying Equation (8), thereby assuming that all pores are spherical but with different initial volumes. Such predictions are shown by

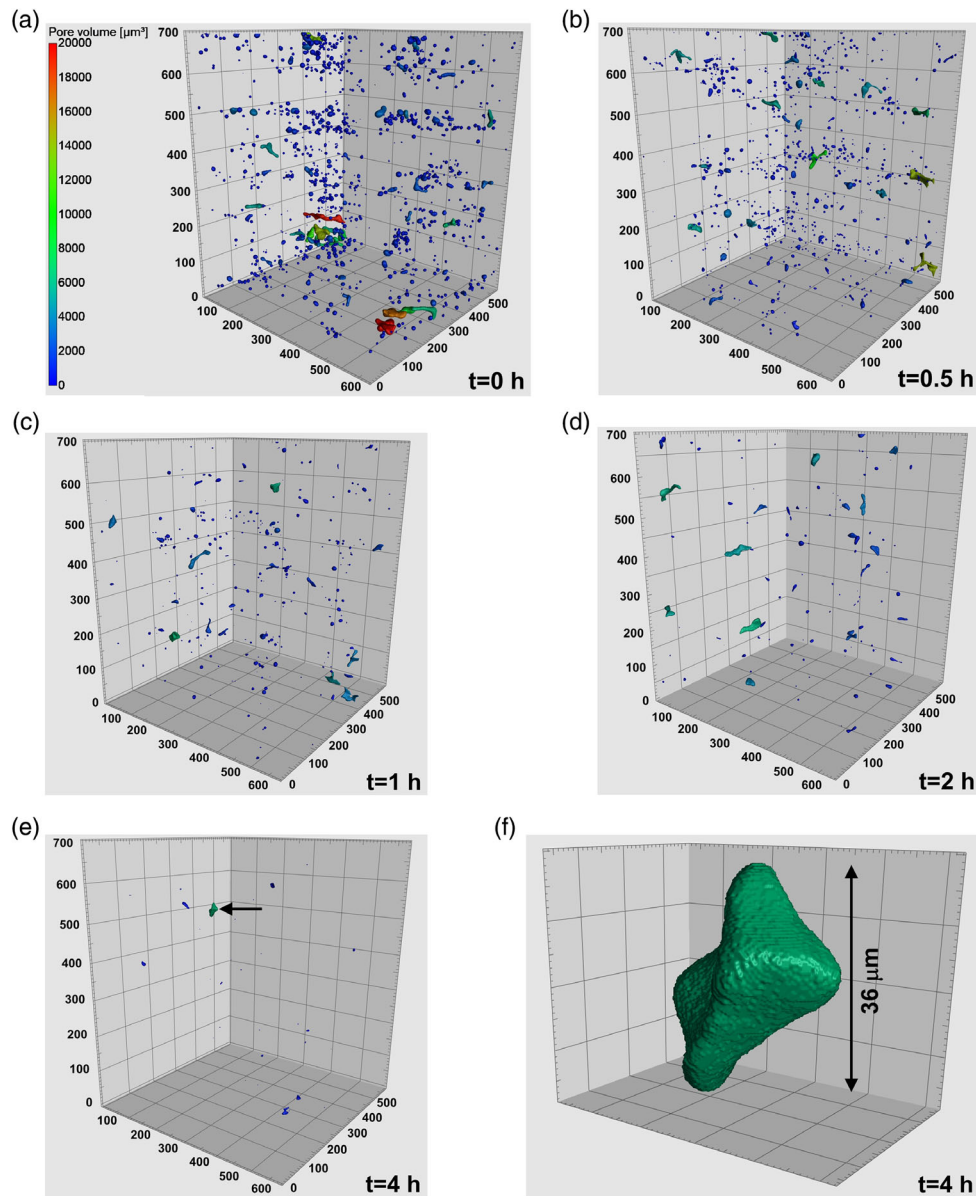


**Figure 3.** a–e) Synchrotron tomography of microporosity in the initially homogenized CMSX-4 after 0, 0.5, 1, 2, and 4 h HIP at 1288 °C and 103 MPa, respectively. f) A pore marked by an arrow in (e) at higher magnification.

the red dashed lines. It is seen that the predicted lines are now closer to the DM and XCT measurements but underestimate the porosity annihilation rate. The best agreement with the experimental results is obtained under the assumption that the pores originally have different volumes and that their shape can deviate from the spherical shape, as described in Equation (9). It is seen that the red solid lines predicted with Equation (9) are closer to the DM and XCT results than the predictions with Equation (7) and (8).

**Figure 5** shows the evolution of the histograms of the equivalent diameters  $D_p^{eq}$  during HIP of the initially homogenized CMSX-4. Figure 5a shows the experimental histograms obtained by processing the porosity tomograms after 0, 0.5, 1, 2, and 4 h HIP at 1288 °C and 103 MPa, see Figure 3a–e. Figure 5b shows the corresponding histograms predicted by applying Equation (9)

to each observed pore in tomogram in Figure 3a and cumulating the results. One can recognize a clear similarity of the experimental and predicted histograms. At  $t = 0$  h, the  $D_p^{eq}$  distribution has a maximum at  $D_p^{eq} \approx 10 \mu\text{m}$  and it is positively skewed. But with increasing HIP, the shape of the  $D_p^{eq}$  distribution changes. The distribution peak progressively decreases and after 2 h HIP, the  $D_p^{eq}$  distribution flattens and becomes negatively skewed. Such a histogram evolution results from the size dependence of the pore shrinking rate. From Equation (9)

$$V_{p,i}(t)/V_{p,i}(0) = \left[1 - \psi_{p,i}^{-1}(0)k_V t/V_{p,i}^{2/3}(0)\right]^{3/2} \quad (10)$$

It is seen from Equation (10) that the relative reduction of the pore volume  $V_{p,i}(t)/V_{p,i}(0)$  increases with decreasing initial pore

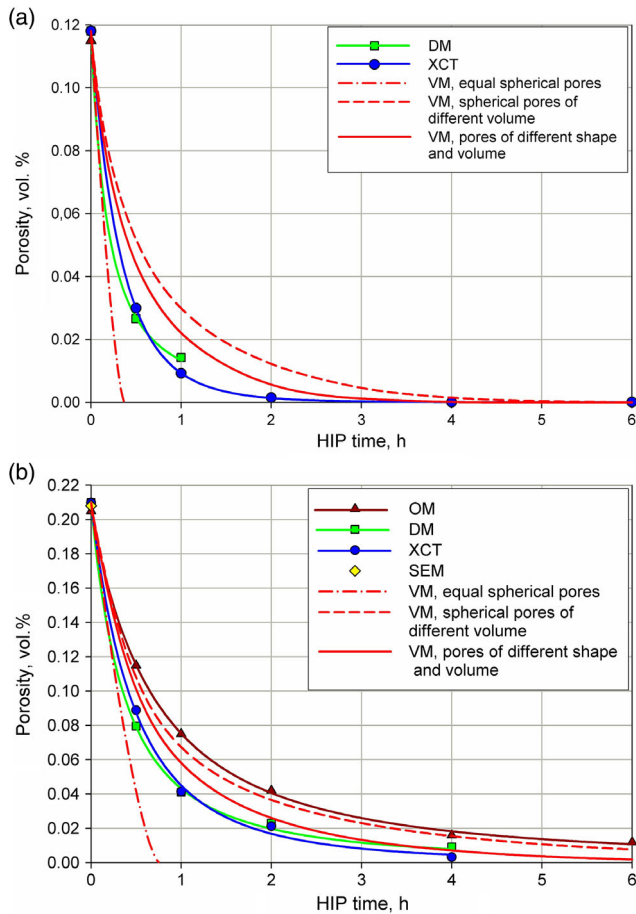


**Figure 4.** Decrease in porosity volume fraction in CMSX-4 during HIP at 1288 °C and 103 MPa, experimentally measured and predicted by the VM. The measurement and the predictions methods are indicated in the legends. a) Initially as cast. b) Initially homogenized.

volume  $V_{p,i}(0)$ . Therefore, the numerous small pores rapidly annihilate, whereas the rare large pores slowly shrink. Consequently, the left part of the  $D_p^{eq}$  histogram is reduced faster than its right part.

However, the experimental and predicted histograms show a discrepancy for large pores. After 1 h, the experimental histogram in Figure 5a does not contain any large pores with  $D_p^{eq} > 25 \mu\text{m}$ , whereas the predicted histogram in Figure 5b still includes such large pores. The first possible reason for this is experimental: the experimental histograms have been measured in different unHIPed and HIPed samples, whereas all theoretical histograms are predicted on the basis of measurements made in a single unHIPed sample. Therefore, the predicted histograms inherit all features of this particular source tomogram. This unHIPed sample contained several large pores including a very large one with  $D_p^{eq} \approx 43.5 \mu\text{m}$ . According to the prediction, this pore gradually shrinks to 43.5, 42.3, 41.1, 38.4, and 32.6  $\mu\text{m}$  diameter after 0, 0.5, 1, 2, and 4 h of HIP duration, respectively. This single pore corresponds to the last gray, then yellow, green, blue, and finally red bar on the right side of the histogram in Figure 5b. The second possible reason for this discrepancy could

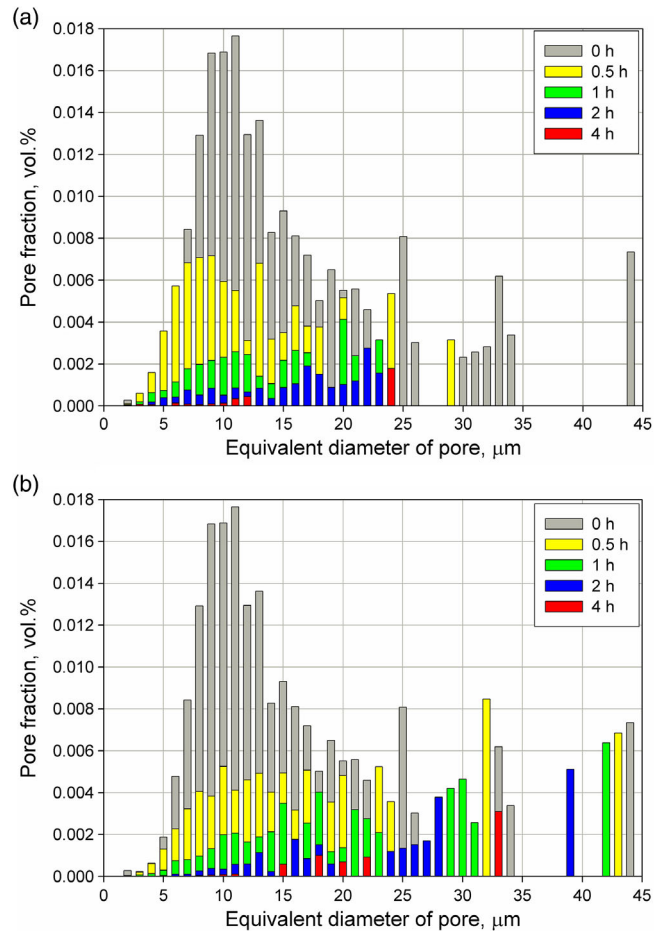


**Figure 5.** Histograms of the equivalent pore diameters in the initially homogenized CMSX-4 after 0, 0.5, 1, 2, and 4 h HIP at 1288 °C and 103 MPa. a) Experimental histograms corresponding to the porosity tomograms shown in Figure 3a–e. b) Histograms predicted for  $t = 0.5, 1, 2,$  and 4 h with the refined VM (Equation (9)) on the basis of the experimental histogram at  $t = 0$  h.

be of a geometrical nature, namely, an underestimation of the inverse sphericity factor  $\psi_{p,i}^{-1}$  for large pores by the approach<sup>[31]</sup> expressed by the Equations (2–4). The corresponding correction yields a correct value of the inverse sphericity  $\psi_{p,i}^{-1} = 1$  for a sphere, but for other 3D shapes  $\psi_{p,i}^{-1}$  is generally underestimated. For example, for a cuboid with edges parallel to the coordinated axes  $x, y, z$  or a thin plate normal to one of these axes,  $\psi_{p,i}^{-1}$  is underestimated by a factor of two-thirds. The degree of underestimation of  $\psi_{p,i}^{-1}$  is especially high for the nonconvex shapes with a developed surface, e.g., like a great icosahedron, which is also the case of large S pores, see Figure 1. Therefore, for reliable prediction of the evolution of large pores during HIP, a precise determination of  $\psi_{p,i}^{-1}$  is needed.

An important information for the applications is the pressure dependence of the porosity annihilation rate, because it facilitates the selection of optimal HIP parameters. Moreover, the corresponding experimental data can be used for validation of the proposed HIP models. To determine the pressure dependence of the porosity annihilation rate, several HIP experiments of duration

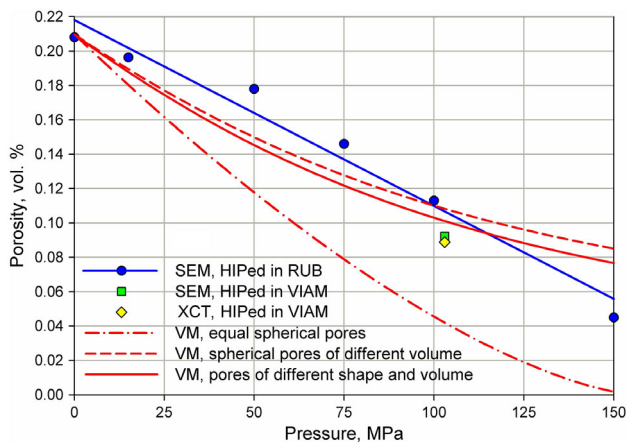


**Figure 6.** Volume fraction of the porosity in the initially homogenized CMSX-4 after 0.5 h of HIP experiments at 1288 °C conducted under pressures between 15 and 150 MPa. Symbols and the blue line are experimental results. Red lines are predicted by the VM: dashed–dotted line for equal spherical pores, dashed line for spherical pores of different volume, and solid line for pores of different shape and volume.

0.5 h have been conducted at 1288 °C and under pressures between 15 and 150 MPa with the initially homogenized CMSX-4. The porosity measurements by different methods and for the standard pressure 103 MPa are shown in **Figure 6** by symbols, whereas SEM measurements for the different pressures are indicated by blue circles and a blue line for the corresponding linear regression.

It is seen that the values of residual porosity  $f_p(0.5 \text{ h}, 100 \text{ MPa})$  measured by SEM in the samples HIPed under the pressure of 100 MPa at the RU Bochum and the values  $f_p(0.5 \text{ h}, 103 \text{ MPa})$  measured by SEM and XCT in the samples HIPed under 103 MPa at the VIAM Moscow are close to 0.1 vol%. The similarity of the results from independent experiments testifies the reliability of the conducted HIP tests and the following porosity characterization. The fitting of the SEM results obtained for the samples HIPed at RUB Bochum (blue circles) reveals a nearly linear dependence (blue line) on the applied pressure  $p$ . The red lines in Figure 6 are predictions with the VM conducted under different assumptions. Again, it is observed that assuming equal volume spherical pores (red dashed–dotted line) leads to faster pore annihilation than in the experiment. The predictions under the assumptions of spherical pores with different initial volumes (red dashed line) and pores of different shapes and initial volumes (red solid line) are generally in agreement with the experimental results.

#### 4. Discussion

HIP experiments conducted with the superalloy CMSX-4 have allowed us to refine and validate a previously proposed VM of porosity annihilation. The model properly predicts the time dependence  $f_p(p = 103 \text{ MPa}, t)$  for HIP at 1288 °C under the pressure of 103 MPa as well as the stress dependence  $f_p(t = 0.5 \text{ h}, p)$  within the pressure range between 15 and 100 MPa. However, at pressure levels higher than 100 MPa, the

experimental and predicted curves  $f_p(t = 0.5 \text{ h}, p)$  tend to diverge, see Figure 6. Thus, with increasing pressure, it is likely that another HIP mechanism becomes dominant, e.g., pore closure by dislocation creep, as modeled in various studies.<sup>[22,25]</sup>

For validation of the VM, it was necessary to couple it with synchrotron X-ray tomography. The best predictions could be obtained under the most realistic assumption that the pores initially have different shapes and volumes. The use of the VM for animation of the experimental porosity tomograms, and showing how the porosity should evolve during HIP, could be proposed as future development of this experimental–modeling combination.

In this work, we have applied high-resolution submicron synchrotron X-ray tomography to characterize small and large pores. This was necessary to verify the hypothesis of pore closure by vacancy diffusion and validate the proposed computational model. So, this investigation has both academic and practical importance. However, the use of high-resolution synchrotron tomography in practical work is not possible for two reasons. First, it is very expensive. Second, it needs small samples, as described in Experimental Section, and therefore cannot be applied to full-scale components. However, for practical purposes, such a high resolution is unnecessary because the critical pores are large, see Figure 1a. Fractographic inspection of single crystals of CMSX-4 ruptured at 700 °C during low fatigue tests conducted by BAM Berlin showed that in all samples the fatigue cracks nucleated from such large S pores.<sup>[5]</sup> Therefore, for practice, it is suggested to combine lower-resolution X-ray tomography of large samples with laboratory equipment with validated vacancy modeling. Based on the tomography characterization of large pores, one could then simulate their evolution during HIP under different conditions and analyze the results to select the optimal HIP parameters for porosity healing. An additional benefit of this procedure is that the analysis of larger samples would improve the statistical characterization of large pores.

In spite of the observed consistency between the theoretical predictions and the experimental results, the VM obviously should be further refined as follows. 1) The effect of pore shape on the shrinking rate should be analyzed in detail. It is relevant for large pores of irregular shape, which are critical defects of single-crystal superalloys. 2) The effect of multicomponent diffusion should be understood, too. It is often considered by introducing the so-called “effective diffusion coefficient”  $D_{\text{eff}}^{\text{Ni}}$ , as discussed in the study by Zhu et al.<sup>[38]</sup> However, such an approach raises questions. For example, the simple arithmetic averaging of the diffusion coefficients  $D_X^{\text{Ni}}(1288 \text{ °C})$  of the elements alloyed in CMSX-4 ( $D_{\text{Re}}^{\text{Ni}}$  from the study by Epishin et al.<sup>[39]</sup> and other  $D_X^{\text{Ni}}$  from the study by<sup>[35]</sup>) with factors equal to their atomic fractions (Table 1) leads to  $D_{\text{Ni}}^{\text{Ni}}(1288 \text{ °C}) = 8.46 \times 10^{-14} \text{ m}^2 \text{ s}^{-1}$ . This value obtained for CMSX-4 alloyed by refractory elements is higher than the self-diffusion coefficient of nickel  $D_{\text{Ni}}^{\text{Ni}}(1288 \text{ °C}) = 5.62 \times 10^{-14} \text{ m}^2 \text{ s}^{-1}$  following from the results of the study by Engstrom et al.<sup>[35]</sup> and used in this work. In the study by Zhu et al.<sup>[38]</sup> it is proposed to calculate  $D_{\text{eff}}^{\text{Ni}}$  in two ways, including arithmetic averaging of the diffusion activation energies  $Q_X^{\text{Ni}}$  and harmonic or arithmetic averaging of the pre-exponential factors  $D_{0,X}^{\text{Ni}}$  in the temperature dependences of diffusion coefficients  $D_X^{\text{Ni}}(T)$ . These calculations lead to  $D_{\text{eff}}^{\text{Ni}}$  values that differ by an order of magnitude. Obviously,

$D_{\text{eff}}^{\text{Ni}}$  cannot be defined by a general rule for any alloy because it not only depends on the alloy composition but also on the specific diffusion problem under consideration. For example, it was shown that the alloying elements in nickel-base superalloys significantly interact during interdiffusion and therefore the overall diffusion process can accelerate or slow down depending on the mutual directions of the diffusion fluxes.<sup>[40,41]</sup> Thus, it is suggested to assess the impact of multicomponent diffusion on pore shrinkage by directly solving the multicomponent diffusion problem with a diffusion simulation software like, e.g., DICTRA.<sup>[42]</sup> In turn, from the results of such computationally more demanding simulations, specific effective diffusion coefficients can be identified for use in fast calculations. 3) Finally, additional pore closure mechanisms should be also considered. The most probable second mechanism of pore closure is dislocation creep, as it was modeled.<sup>[22,25]</sup> Therefore, the dislocation creep model should be refined and coupled with the VM, which would extend the predictive capacity of modeling to a wider field of the HIP parameters.

## 5. Conclusion

1) Annihilation of microporosity in initially as-cast and in homogenized single crystals of nickel-base superalloy CMSX-4 during HIP at 1288 °C has been characterized by metallographic methods and by high-resolution submicron synchrotron tomography. The time and pressure dependencies of the annihilation kinetics have been obtained. 2) On the base of the obtained experimental results, the previously proposed VM of porosity annihilation has been improved and validated. This model refinement was made possible by identifying the proper initial conditions via X-ray tomography measurements of the initial pore volumes and shapes. The model describes the evolution of the porosity array present in a tomogram during HIP and properly predicts the kinetics of pore annihilation and its pressure dependence. 3) The obtained experimental and numerical results have demonstrated that porosity healing in CMSX-4 during HIP at 1288 °C and pressures up to about 100 MPa occurs via pore dissolution by vacancy emission and diffusion. The experimental results and the VM can be used for the optimization of the parameters (pressure and time) of commercial HIP of single-crystal superalloy CMSX-4 or comparable alloys with low volume fraction of porosity up to about 0.3–0.4 vol%. This is due to neglecting diffusional interaction between the pores and describing the annihilation of pores during HIP considering every pore independently.

## Acknowledgements

The authors acknowledge the European Synchrotron Radiation Facility (ESRF) in Grenoble for provision of synchrotron radiation facilities and thank Mrs. Elodie Boller for assistance in using beamline ID19 and Mr. Romeo Saliwan Neumann, BAM Berlin, for assistance in scanning electron microscopy (SEM) imaging. This work was supported by the German Research Foundation (DFG), projects EP 136/1-1, FE933/2-1, and subproject T4 of SFB/TR 103.

Open access funding enabled and organized by Projekt DEAL.

## Conflict of Interest

The authors declare no conflict of interest.

## Data Availability Statement

Research data are not shared.

## Keywords

diffusion modeling, hot isostatic pressing, nickel alloys, porosity, X-ray synchrotron tomography

Received: February 18, 2021

Revised: March 22, 2021

Published online:

- [1] R. C. Reed, *The Superalloys: Fundamentals and Applications*, Cambridge University Press, New York **2006**.
- [2] R. E. Shalin, I. L. Svetlov, E. B. Kachanov, V. N. Toloraja, O. S. Gavrilin, *Single Crystals of Nickel-Base Superalloys*, Moscow **1997**.
- [3] J. Lecomte-Beckers, *Trans. A* **1988**, *19*, 2341.
- [4] V. N. Toloraja, A. G. Zuev, I. L. Svetlov, *Izv. AN. USSR, Metals* **1991**, *5*, 70.
- [5] H. Klingelhöffer, A. Epishin, T. Link, *Mater. Test.* **2009**, *51*, 291.
- [6] D. L. Anton, A. F. Giamei, *Mater. Sci. Eng.* **1985**, *76*, 173.
- [7] B. S. Bokstein, A. I. Epishin, T. Link, A. O. Rodin, I. L. Svetlov, *Scr. Mater.* **2007**, *57*, 801.
- [8] A. Epishin, T. Link, I. L. Svetlov, G. Nolze, R. Saliwan Neumann, H. Lukas, *Inter. J. Mater. Res.* **2013**, *104*, 1.
- [9] R. I. Garber, V. S. Kogan, L. M. Poliakov, *Sov. Phys. JETP* **1959**, *35*, 953.
- [10] J. Komenda, P. J. Henderson, *Scr. Mater.* **1997**, *37*, 1821.
- [11] A. H. Sherry, R. Pilkington, *Mater. Sci.* **1993**, *172*, 51.
- [12] S. H. Ai, V. Lupinc, M. Maldini, *Scr. Metall. Mater.* **1992**, *26*, 579.
- [13] A. Epishin, T. Link, *Philos. Mag.* **2004**, *84*, 1979.
- [14] A. Epishin, T. Link, U. Brückner, P. D. Portella, in *Materials for Advanced Power Engineering, Part 1* (Eds: J. Lecomte-Beckers, M. Carton, F. Schubert, P. J. Ennis), FZ Jülich, Jülich **2002**, 217.
- [15] M. Lamm, A. Volek, O. Luelsebrink, R. F. Singer, in *Materials for Advanced Power Engineering, Part 1* (Eds: J. Lecomte-Beckers, M. Carton, F. Schubert, P. J. Ennis), FZ Jülich, Jülich **2006**, 334.
- [16] L. G. Fritzemeier, in *Superalloys 1988: Proc. of the Sixth Int. Symp. on Superalloys Sponsored by the High Temperature Alloys Committee of the Metallurgical Society* (Eds.: D. N. Duhl), The Society, Warrendale, PA **1988**.
- [17] K. P. L. Fullagar, R. W. Broomfield, M. Hulands, K. Harris, G. L. Erickson, S. L. Sikkenga, *J. Eng. Gas Turbines Power* **1996**, *118*, 380.
- [18] J. C. Chang, Y. H. Yun, C. Choi, J. C. Kim, *J. Mater. Eng. Perform.* **2003**, *12*, 420.
- [19] R. C. Reed, D. C. Cox, C. M. F. Rae, *Mater. Sci. Eng. A* **2007**, *448*, 88.
- [20] F. Ebrahimi, E. F. Westbrooke, *Acta Mater.* **2008**, *56*, 4349.
- [21] L. J. Liu, M. Xue, J. Y. Chen, L. M. Cao, *Mater. Sci. Forum* **2013**, *747–748*, 772.
- [22] A. I. Epishin, T. Link, B. Fedelich, I. L. Svetlov, E. R. Golubovskiy, *MATEC Web Conf.* **2014**, *14*, 088003.
- [23] L. Mujica Roncery, I. Lopez-Galilea, B. Rutttert, S. Huth, W. Theisen, *Mater. Des.* **2016**, *97*, 544.
- [24] L. Mujica Roncery, I. Lopez-Galilea, B. Rutttert, D. Bürger, P. Wollgramm, G. Eggeler, W. Theisen, *Adv. Eng. Mater.* **2016**, *18*, 1381.
- [25] A. Epishin, B. Fedelich, T. Link, T. Feldmann, I. L. Svetlov, *Mater. Sci. Eng. A* **2013**, *586*, 342.
- [26] A. I. Epishin, B. S. Bokstein, I. L. Svetlov, B. Fedelich, T. Feldmann, Y. Le Bouar, A. Ruffini, A. Finel, B. Viguier, D. Poquillon, *Mater. Appl. Res.* **2018**, *9*, 57.



- [27] T. Link, S. Zabler, A. Epishin, A. Haibel, M. Bansal, X. Thibault, *Mat. Sci. Eng. A* **2006**, 425, 47.
- [28] K. Harris, G. L. Erickson, S. L. Sikkenga, W. D. Brentnall, J. M. Aurrecoechea, K. G. Kubarych, *J. Mater. Eng. Perform.* **1993**, 2, 481.
- [29] VGSTUDIO MAX, High-End Industrial CT Software, Version 2.1, <https://www.volumegraphics.com/de/produkte/vgstudio-max.html> (accessed: October 2020).
- [30] H. Wadell, *J. Geol.* **1933**, 41, 310.
- [31] C. Rothleitner, U. Neuschaefer-Rube, J. Illeemann, in *6th Conf. on Industrial Computed Tomography (iCT) 2016*, Springer Science+Business Media LLC, Wels, Austria **2016**, pp. 9–12.
- [32] ImageJ: Image Processing and Analysis in Java, <https://imagej.nih.gov/ij/> (accessed: October 2020).
- [33] S. A. Saltykov, *Stereometric Metallography*, Metallurgizdat, Moscow **1970** (in Russian).
- [34] S. A. Saltykov, *Stereometrische Metallographie*, VEB Deutscher Verlag für Grundstoffindustrie, Leipzig, **1974** (in German).
- [35] A. Engström, J. Ågren, *Zeitschrift für Metallkunde* **1996**, 87, 92.
- [36] J. R. Manning, *Phys. Rev.* **1964**, 136, A1758.
- [37] M. Koiwa, S. Ishioka, *Philos. Mag. A* **1983**, 47, 927.
- [38] Z. Zhu, H. Basoalto, N. Warnken, R. C. Reed, *Acta Mater.* **2012**, 60, 4888.
- [39] A. I. Epishin, A. O. Rodin, B. S. Bokstein, G. Oder, T. Link, *Metallogr.* **2015**, 116, 175.
- [40] A. Chyrkin, A. Epishin, R. Pillai, T. Link, G. Nolze, W. J. Quadackers, *J. Phase Equilib. Diff.* **2016**, 37, 201.
- [41] A. Epishin, A. Chyrkin, B. Camin, R. Saillard, S. Gouy, B. Viguier, *Diffus. Defect Forum* **2021**, 407, 1.
- [42] J. O. Andersson, T. Helander, L. Höglund, P. Shi, B. Sundman, *Calphad* **2002**, 26, 273.